In Situ Built Nanoconfined Nb_2O_5 Particles in 3D Interconnected Nb_2C MXene@rGO Conductive Framework for High-Performance Potassium-Ion Batteries

*Cong Liu,[a,b] Zhitang Fang,[a] Weizhi Kou,[a] Xiaoge Li,[c] Jinhua Zhou,[d] Gang Yang,[d] Luming Peng,[a] Xuefeng Guo,[a] Weiping Ding,[a] Wenhua Hou[a]**

[a] Key Laboratory of Mesoscopic Chemistry of MOE, School of Chemistry and Chemical Engineering, Nanjing University, Nanjing, 210023, P. R. China.

[b] School of Materials Engineering, Jiangsu University of Technology, Changzhou 213001, P.R. China.

[c] School of Chemistry and Chemical Engineering, Yangzhou University, Yangzhou, 225009, P. R. China.

[d] Suzhou Key Laboratory of Functional Ceramic Materials, Changshu Institute of Technology, Changshu, 215500, P. R. China.

* Corresponding author.

E-mail address: whou@nju.edu.cn (W. Hou)

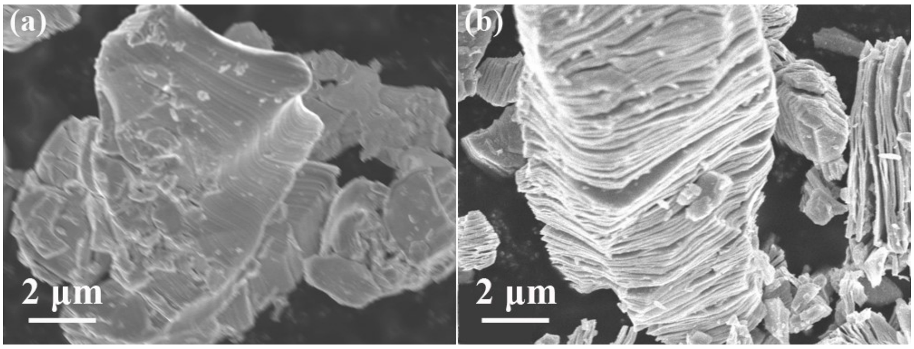

Figure S1 Typical SEM images of (a) Nb_2AlC and (b) multi-layered Nb_2CT_x.

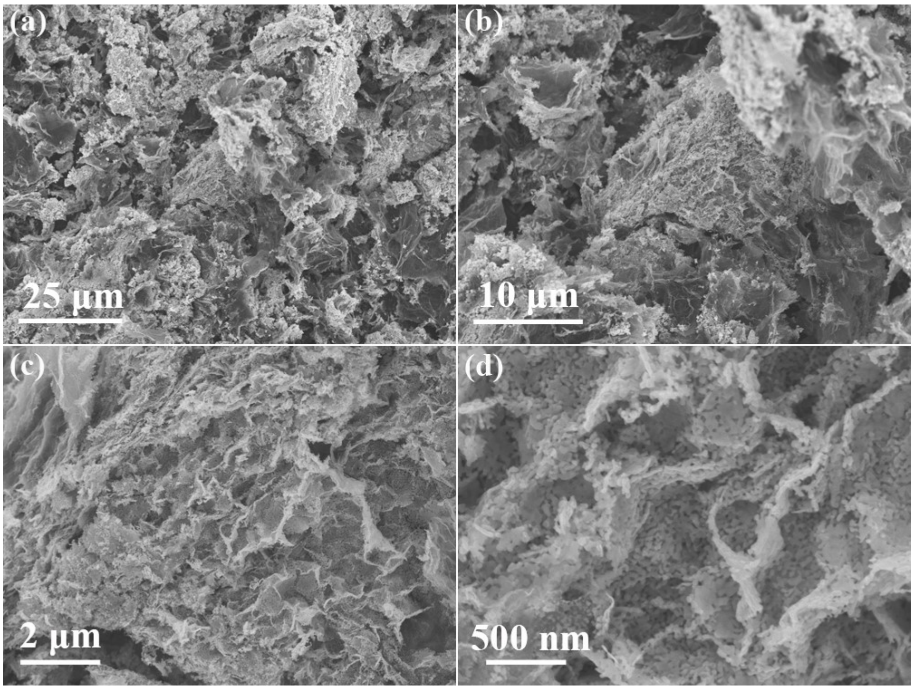

Figure S2 Typical SEM images of Nb_2O_5/rGO.

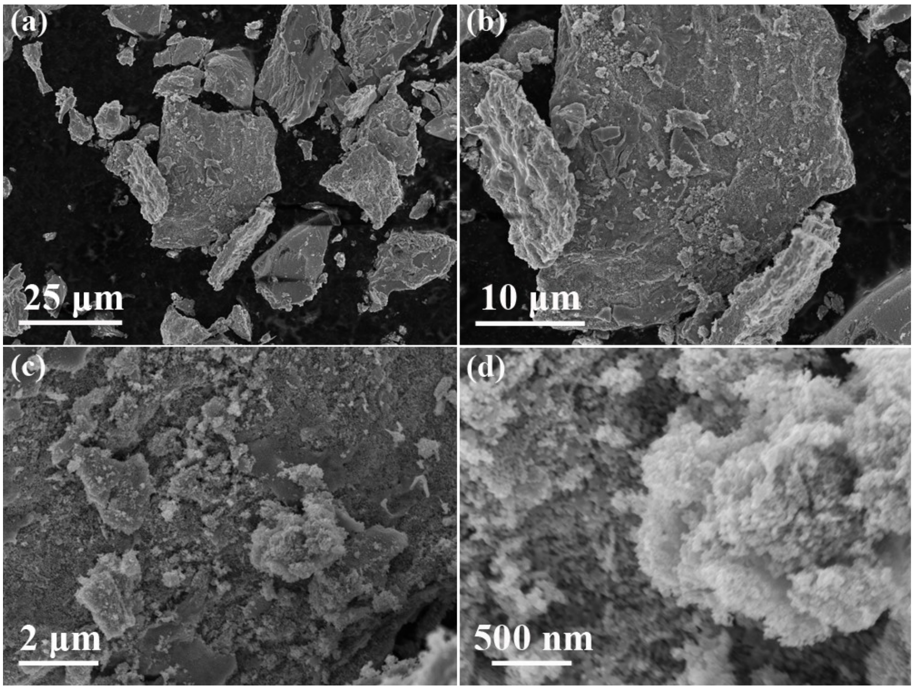

Figure S3 Typical SEM images of Nb_2O_5.

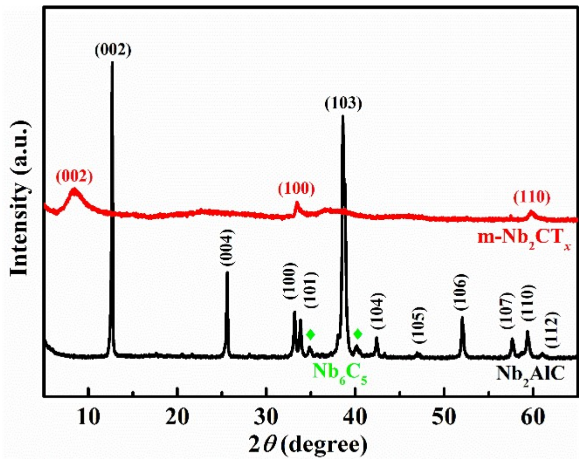

Figure S4 XRD patterns of Nb_2AlC and m-Nb_2CT_x.

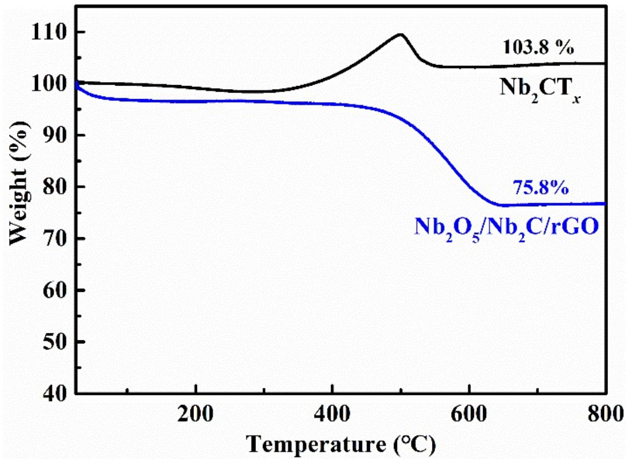

Figure S5 TGA curves of Nb_2CT_x nanosheets and Nb_2O_5/Nb_2C/rGO aerogel.

As shown in **Fig. S5**, the final stable weights of Nb_2CT_x nanosheets and Nb_2O_5/Nb_2C/rGO are 103.8 wt% and 75.8 wt%, respectively. The weight change of pureNb_2CT_x nanosheets is (103.8–100) wt%=+3.8 wt%. The weight change of Nb_2O_5/Nb_2C/rGO is (75.8–100) wt%= –24.2 wt%. There is no doubt that the weight change of pure rGO is –100 wt% (*i.e.*, fully oxidized/decomposed into gaseous products). Therefore, the content of rGO in Nb_2O_5/Nb_2C/rGO can be calculated based on the formula $(1–A)\times3.8\%–A\times100\%=B$, where A is the content of rGO in Nb_2O_5/Nb_2C/rGO, and B is the weight change of Nb_2O_5/Nb_2C/rGO (*i.e.*, –24.2 wt%). Hence, according to TGA results, the content of rGO in Nb_2O_5/Nb_2C/rGO sample is calculated to be 27.0 wt%.

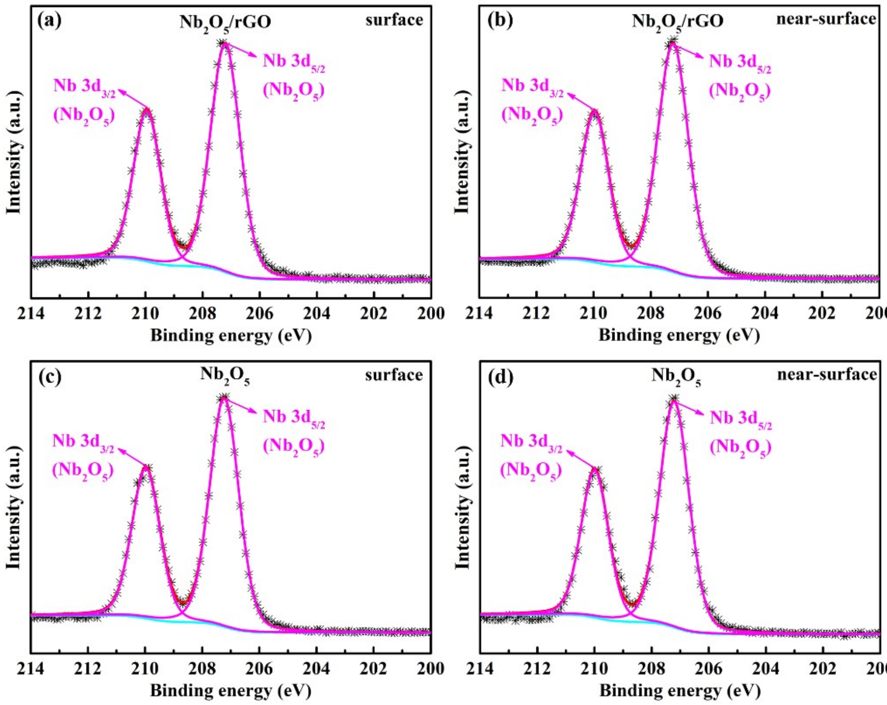

Figure S6 Refined high-resolution Nb 3d XPS spectra of (a, b) Nb_2O_5/rGO and (c, d) Nb_2O_5 before (a, c) and after (b, d) Ar^+ ion sputtering.

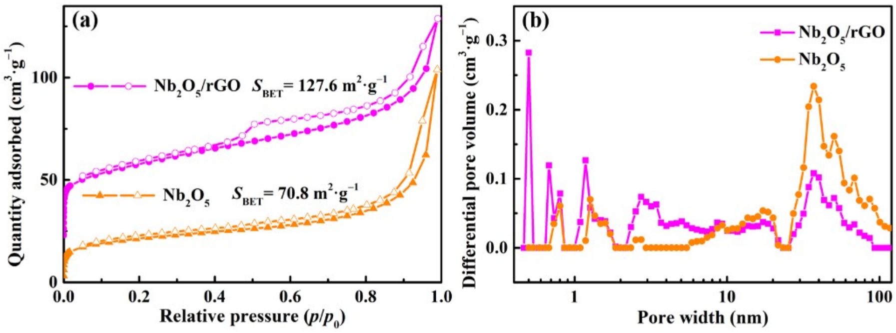

Figure S7 (a) N_2 adsorption and desorption isotherms and (b) the corresponding pore-size distribution curves of Nb_2O_5/rGO and Nb_2O_5.

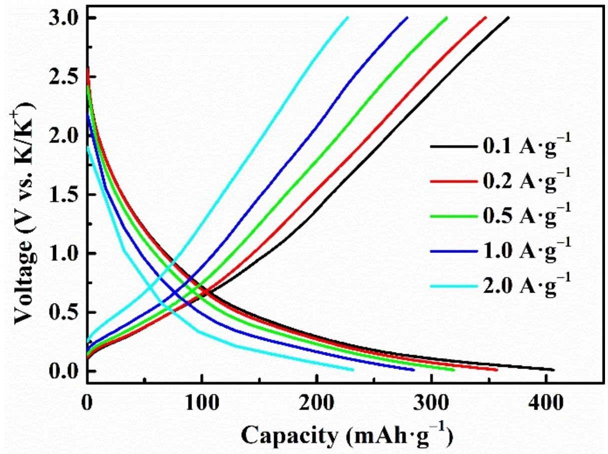

Figure S8 GCD curves of Nb_2O_5/Nb_2C/rGO at different current densities.

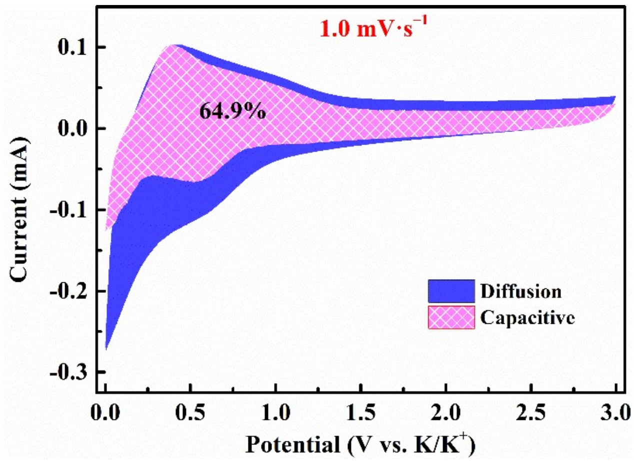

Figure S9 Capacitive- and diffusion-controlled contributions at 1.0 mV·s^{-1} for the Nb_2O_5/Nb_2C/rGO.

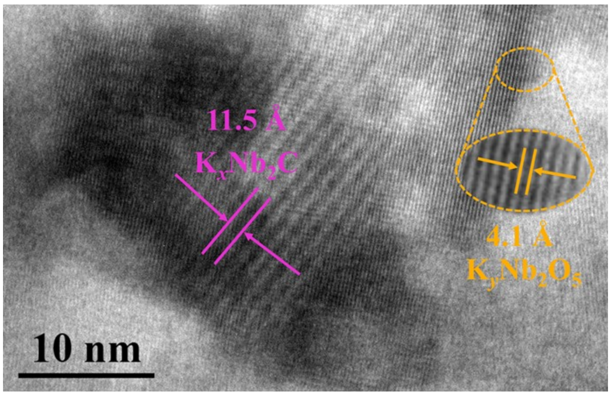

Figure S10 HRTEM of Nb_2O_5/Nb_2C/rGO electrode after being discharged to 0.01V.

HRTEM test was performed on the electrode after being discharged to 0.01 V to confirm the evolution of structure. As shown in **Figure 2i** and **Figure S10**, it can be observed that the interlayer distance of Nb_2C is increased from 10.4 to 11.5 Å and that of Nb_2O_5 is increased from 3.9 Å to 4.1 Å, indicating that K^+ is successfully intercalated into Nb_2C and Nb_2O_5 layers and thus the formation of K_xNb_2C and $K_yNb_2O_5$.

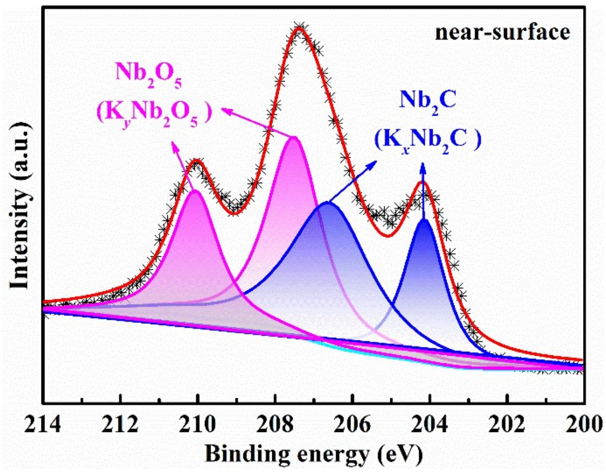

Figure S11 Nb 3d XPS spectrum for the near-surface of Nb_2O_5/Nb_2C/rGO.

As shown in **Figure S11**, the near-surface of Nb_2O_5/Nb_2C/rGO exhibits four peaks at 210.0, 207.3, 206.4 and 204.1 eV, respectively. Combined with **Figure 5e**, the first two peaks are assigned to Nb_2O_5 ($K_yNb_2O_5$), while the last two peaks can be indexed to Nb_2C (K_xNb_2C).

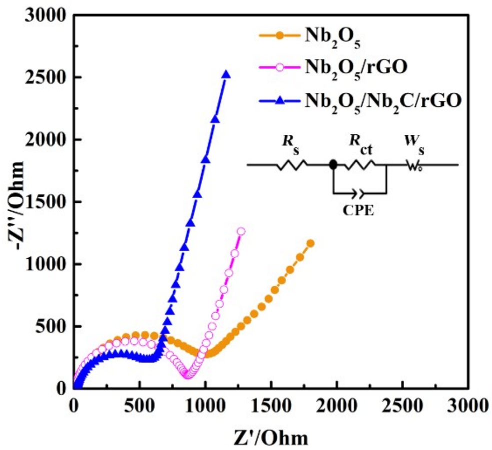

Figure S12 EIS spectra for $Nb_2O_5/Nb_2C/rGO$, Nb_2O_5/rGO and Nb_2O_5.

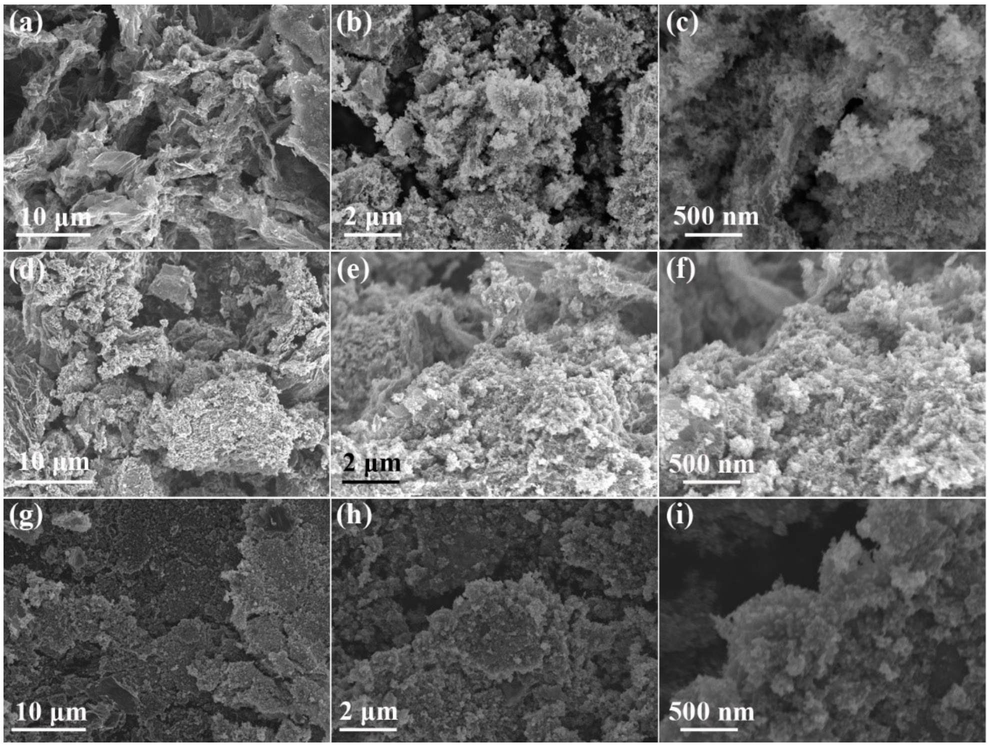

Figure S13 SEM images of (a-c) $Nb_2O_5/Nb_2C/rGO$, (d-f) Nb_2O_5/rGO and (g-i) Nb_2O_5 electrodes after 100 cycles at a current density of $0.1A\cdot g^{-1}$.

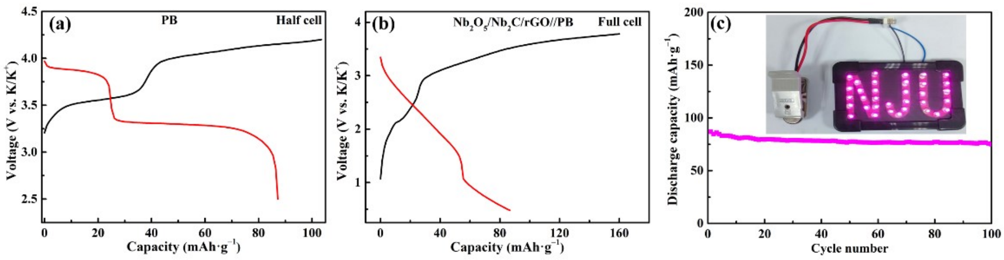

Figure S14 GCD curves of (a) PB in half-cell and (b) Nb_2O_5/Nb_2C/rGO//PB full-cell at a current density 0.1 A·g^{-1}; (c) cycle performance of Nb_2O_5/Nb_2C/rGO//PB full-cell at a current density of 0.1 A·g^{-1} (inset shows LEDs powered by the full cell).

PB was prepared by a simple precipitation method. **Figure S14a** shows the GCD curves of PB in half-cell with charge and discharge capacities of 103.5 and 87.2 mAh·g^{-1}, respectively. Before assembling the full-cells, the charge balance between anode and cathode needs to be optimized by controlling the mass ratio of anode and cathode based on the specific discharge capacities of Nb_2O_5/Nb_2C/rGO and PB in half-cells.

Table S1 A detailed comparison of the electrochemical performance of different anode materials for KIBs.

Samples	Capacity ($mA \cdot g^{-1}$) @rate ($A \cdot g^{-1}$)	Capacity retention @rate ($A \cdot g^{-1}$)@cycles	Ref.
Sn/rGO	222.4 @ 0.1 67.1 @ 2	69% @ 0.5 @ 500	[1]
MoS_2/graphene	511 @ 0.1 234 @ 2	75% @ 1 @ 800	[2]
N-Doped graphene	320 @ 0.05 170 @ 0.5	88% @ 0.5 @ 500	[3]
TiO_xN_y/C	150 @ 0.2 75 @ 1.6	23% @ 0.2 @ 120	[4]
Onion-like carbon	245 @ 0.05 78 @10	71% @ 2 @ 980	[5]
TiS_2	124 @ 0.05 92.1 @ 0.25	64% @ 0.05 @ 450	[6]
Co_3O_4-F_2O_3/C	420 @ 0.05 278 @ 1	60% @ 0.05 @ 100	[7]
$KTiOPO_4$	102 @ 0.005 50 @ 0.2	77% @ 0.005 @ 200	[8]
BiOCl	367 @ 50 175 @ 1	58% @ 0.05 @ 50	[9]
Sn_4P_3/MGS	378 @ 0.1 113 @ 5	77% @ 0.5 @ 1000	[10]
Nb_2O_5/Nb_2C/rGO-2	410 @ 0.1 230 @ 2	89% @ 2 @ 1000	This work

References:

[1] Wang, H.; Xing, Z.; Hu, Z.; Zhang, Y.; Hu, Y.; Sun, Y.; Ju, Z.; Zhuang, Q. Sn-based submicron-particles encapsulated in porous reduced graphene oxide network: Advanced anodes for high-rate and long life potassium-ion batteries. *Appl. Mater. Today*, **2019**, *15*, 58.

[2] Yao, K.; Xu, Z.; Ma, M.; Li, J.; Lu, F.; Huang, J. Densified metallic MoS_2/graphene enabling fast potassium-ion storage with superior gravimetric and volumetric capacities. *Adv. Funct. Mater.*, **2020**, *30*, 2001484.

[3] Ju, Z.; Li, P.; Ma, G.; Xing, Z.; Zhuang, Q.; Qian, Y. Few layer nitrogen-doped graphene with highly reversible potassium storage. *Energy Storage Mater.*, **2018**, *11*, 38.

[4] Tao, M.; Du, G.; Zhang, Y.; Gao, W.; Liu, D.; Luo, Y.; Jiang, J.; Bao, S.; Xu, M. TiO_xN_y nanoparticles/C composites derived from MXene as anode material for potassium-ion batteries. *Chem. Eng. J.*, **2019**, *369*, 828.

[5] Chen, J.; Yang, B.; Li, H.; Ma, P.; Lang, J.; Yan, X. Candle soot: onion-like carbon,

an advanced anode material for a potassium-ion hybrid capacitor. *J. Mater. Chem. A*, **2019**, *7*, 9247.

[6] Liu, T.; Zhang, X.; Xia, M.; Yu, H.; Peng, N.; Jiang, C.; Shui, M.; Xie, Y.; Yi, T.-F.; Shu, J. Functional cation defects engineering in TiS_2 for high-stability anode. *Nano Energy*, **2020**, *67*, 104295.

[7] Sultana, I.; Rahman, M. M.; Mateti, S.; Ahmadabadi, V. G.; Glushenkov, A. M.; Chen, Y. K-ion and Na-ion storage performances of Co_3O_4-Fe_2O_3 nanoparticle-decorated super P carbon black prepared by a ball milling process. *Nanoscale*, **2017**, *9*, 3646.

[8] Zhang, R.; Huang, J.; Deng, W.; Bao, J.; Pan, Y.; Huang, S.; Sun, C. F. Safe, Low-Cost, Fast-kinetics and low-strain inorganic-open-framework anode for potassium-ion batteries. *Angew. Chem. Int. Ed.*, **2019**, *58*, 16474.

[9] Wang, J.; Wang, B.; Lu, B. Nature of novel 2D van der Waals heterostructures for superior potassium ion batteries. *Adv. Energy Mater.*, **2020**, *10*, 2000884.

[10] Du, Y.; Yi, Z.; Chen, B.; Xu, J.; Zhang, Z.; Bao, J.; Zhou, X. Sn_4P_3 nanoparticles confined in multilayer graphene sheets as a high-performance anode material for potassium-ion batteries. *J. Energy Chem.*, **2022**, *66*, 413.